SMALL-SCALE STRUCTURE OF THE SN 1006 SHOCK WITH *CHANDRA* OBSERVATIONS

AYA BAMBA, RYO YAMAZAKI, MASARU UENO, AND KATSUJI KOYAMA

Department of Physics, Graduate School of Science, Kyoto University, Sakyo-ku, Kyoto 606-8502, Japan;
bamba@cr.scphys.kyoto-u.ac.jp, yamazaki@tap.scphys.kyoto-u.ac.jp, masaru@cr.scphys.kyoto-u.ac.jp,
koyama@cr.scphys.kyoto-u.ac.jp

ABSTRACT

The northeast shell of SN 1006 is the most probable acceleration site of high-energy electrons (up to $\sim$100 TeV) with the Fermi acceleration mechanism at the shock front. We resolved nonthermal filaments from thermal emission in the shell with the excellent spatial resolution of *Chandra*. The thermal component is extended over $\sim$100″ (about 1 pc at 1.8 kpc distance) in width, consistent with the shock width derived from the Sedov solution. The spectrum is fitted with a thin thermal plasma of $kT = 0.24$ keV in nonequilibrium ionization, typical for a young supernova remnant. The nonthermal filaments are likely thin sheets with scale widths of $\sim$4″ (0.04 pc) and $\sim$20″ (0.2 pc) upstream and downstream, respectively. The spectra of the filaments are fitted with a power-law function of index 2.1–2.3, with no significant variation from position to position. In a standard diffusive shock acceleration model, the extremely small scale length in the upstream region requires the magnetic field nearly perpendicular to the shock normal. The injection efficiency (η) from thermal to nonthermal electrons around the shock front is estimated to be $\sim 1 \times 10^{-3}$ under the assumption that the magnetic field in the upstream region is 10 μG. In the filaments, the energy densities of the magnetic field and nonthermal electrons are similar to each other, and both are slightly smaller than that of thermal electrons. These results suggest that the acceleration occurs in more compact regions with larger efficiency than suggested by previous studies.

Subject headings: acceleration of particles — ISM: individual (SN 1006) — shock waves — supernova remnants — X-rays: ISM

1. INTRODUCTION

Since the discovery of cosmic rays (Hess 1912), the origin and acceleration mechanism up to $10^{15.5}$ eV (the "knee" energy) have been long-standing problems. A breakthrough came from the X-ray studies of SN 1006; Koyama et al. (1995) discovered synchrotron X-rays from the shells of this supernova remnant (SNR), indicating the existence of extremely high energy electrons up to the knee energy produced by the first-order Fermi acceleration. Further, Tanimori et al. (1998) confirmed the presence of high-energy electrons with the detection of the TeV γ-rays, which are cosmic microwave photons up-scattered by high-energy electrons (the inverse Compton process) in the northeast shell of SN 1006. The combined analysis of the synchrotron X-rays and inverse Compton TeV γ-rays nicely reproduces the observed flux and spectra and predicts a rather weak magnetic field of 4–6 μG (Tanimori et al. 1998, 2003).

Since these discoveries, detection of synchrotron X-rays and/or TeV γ-rays from other shell-like SNRs has been accumulating: G347.3$-$0.5 (Koyama et al. 1997; Slane et al. 1999; Muraishi et al. 2000; Enomoto et al. 2002), RCW 86 (Bamba, Tomida, & Koyama 2000; Borkowski et al. 2001b), and G266.6$-$1.2 (Slane et al. 2001). These discoveries provide good evidence for the cosmic ray acceleration at the shocked shell of SNRs. The mechanism of cosmic ray acceleration has also been studied for a long time, and the most plausible process is a diffusive shock acceleration (DSA) (Bell 1978; Blandford & Ostriker 1978; Drury 1983; Blandford & Eichler 1987; Jones & Ellison 1991; Malkov & Drury 2001).

Apart from the globally successful picture of DSA, detailed but important processes, such as the injection, magnetic field configuration, and the reflection of accelerated particles, are not yet well understood. The spatial distribution of accelerated particles responsible for the nonthermal X-rays may provide key information on these unclear subjects. Previous observations, however, do not have sufficient spatial resolution for a detailed study of the structure of shock acceleration process and injection efficiency. Although many observations and theoretical models exist for SN 1006, these problems are still open issues (Reynolds 1998; Aharonian & Atoyan 1999; Vink et al. 2000; Ellison, Berezhko, & Baring 2000; Dyer et al. 2001; Allen, Petre, & Gotthelf 2001; Berezhko, Ksenofontov, & Völk 2002).

In this paper, we report on the first results of the spectral and spatial studies of the thermal and nonthermal shock structure in the NE shell of SN 1006 with *Chandra* (§ 3). In §§ 4.1 and 4.2, we discuss the spectral analyses and determine the scale widths of the structures for thermal and nonthermal electrons on the basis of a simple DSA with shock-parallel magnetic field. We also derive the injection efficiency (η) of nonthermal electrons from the thermal plasma near the shock front. Based on these results, we discuss possible implications on the DSA process in the NE shell of SN 1006. In this paper, we assume the distance of SN 1006 to be 1.8 kpc (Green 2001).[1]

2. OBSERVATION

We used *Chandra* archival data of ACIS on the northeast shell of SN 1006 (Observation ID 00732) observed on 2000 July 10–11 with the targeted position at (R.A.,

---

[1] Available on the WWW at http://www.mrao.cam.ac.uk/surveys/snrs/.

decl.) $= (15^h03^m51^s6, -41°51'18''8)$. The satellite and instrument are described by Weisskopf, O'Dell, & van Speybroeck (1996) and Garmire et al. (2000), respectively. CCD chips I2, I3, S1, S2, S3, and S4 were used, with the pointing center on S3. Data acquisition from ACIS was made in the timed-exposure faint mode with a readout time of 3.24 s. The data reduction and analyses were made using the *Chandra* Interactive Analysis of Observations (CIAO) software version 2.2.1. Using the Level 2 processed events provided by the pipeline processing at the *Chandra* X-ray Center, we selected *ASCA* grades 0, 2, 3, 4, and 6 as the X-ray events. High-energy electrons due to charged particles and hot and flickering pixels were removed. The effective exposure was $\sim$68 ks for the observation. In this paper, we concentrate on the data of S3 (BI chip), because this chip has the best efficiency in soft X-rays required for the spectral analyses and its on-axis position provides the best point-spread function required for the spatial analysis.

3. ANALYSES AND RESULTS

3.1. *Overall Image*

Figure 1 shows the two-color image from I2, I3, and S1–S4 for the northeast shell of SN 1006. The image is contrasted in the 0.5–2.0 keV band (hereafter, the soft1 band; *red*) and in the 2.0–10.0 keV band (hereafter, the hard band; *blue*) and binned to a resolution of 1″. The fine spatial resolution of *Chandra* unveils extremely narrow filaments in the hard band. They run from north to south along the outer edge of the northeast shell, parallel to the shock fronts observed by Hα emission line (Winkler & Long 1997). These filaments resemble the sheetlike structure of the shock simulated by Hester (1987). The soft1 band image, on the other hand, has a larger scale width, similar to the *ROSAT* HRI image (Winkler & Long 1997). Many clumpy substructures are also seen in this energy band.

3.2. *Inner Shell Region*

To resolve the thermal and nonthermal components, we extracted a spectrum from a bright clump found in the soft1 band image, which is located in the inner part of the northeast shell ("inner region"; Fig. 2, *dashed ellipse*). The background region was selected from a region out of the SNR, as is shown in Figure 2 with dashed lines.

The background-subtracted spectrum shown in Figure 3 has many emission lines. We hence determined the peak energies of the five brightest lines with a phenomenological model, a power-law continuum plus Gaussian lines. The strongest line structures are the peak at 0.55 keV and the hump at 0.67 keV. These energies are nearly equal to those of the Kα and Lyα lines of He- and H-like oxygen, and hence are attributable to highly ionized oxygen. Likewise, the other clear peaks at 0.87, 1.31, and 1.76 keV are most likely He-like Kα of Ne, Mg, and Si, respectively. However, in detail all the observed line energies are systematically smaller than those of the relevant atomic data. These apparent energy shifts are usually observed in a young SNR plasma in nonequilibrium ionization (NEI). The "energy shift" in this case is due to the different line ratios of many sublevels and/or different ionization states. The oxygen Lyα is isolated from the other lines of different ionization states, hence the NEI effect gives no energy shift. Still we see apparent down-shift of the observed line energy from that

of the laboratory data. He-like Kα lines are complex, consisting of many fine structures with split energy of at most $\sim$25 eV (for He-like silicon). Although the energy shift of He-like Kα lines due to NEI should be smaller than this split energy, the observed energy shifts are systematically larger than the split energy. We therefore assumed that the apparent energy shifts are due mainly to energy calibration errors, and hence we estimated the gain error with the six brightest lines (He-like C Kα, He-like O Kα and Kβ, He-like Ne Kα, He-like Mg Kα, and He-like Si Kα) and found a 3.8% energy shift. After correcting the gain, we then fitted the spectrum with a thin thermal plasma model in NEI calculated by Borkowski, Lyerly, & Reynolds (2001a). The abundances of C, N, O, Ne, Mg, Si, S, and Fe in the plasma were treated as free parameters, whereas those of the other elements were fixed at the solar values (Anders & Grevesse 1989). The absorption column was calculated using the cross sections by Morrison & McCammon (1983) with the solar abundances. Since this NEI model exhibited systematic data excess at high energy above 2 keV, we added a power-law component, and the fit improved dramatically. Figure 3 and Table 1 show the best-fit models (dashed and solid lines for thermal and power-law components) and parameters, respectively.

Instead of the phenomenological power-law model, we applied *srcut* in the XSPEC package as a more physical model. Details of the *srcut* model fitting are given in § A1. The best-fit $\nu_{\rm rolloff}$ is 9.2(8.6–10.3) $\times 10^{16}$ Hz, with better χ_ν^2 of 389.0/215 than that of the power-law model of 447.9/215 (see Table 1).

We also tried fitting the thermal components with a plane shock model (XSPEC model *vpshock*) plus either a power

TABLE 1
BEST-FIT PARAMETERS OF THE SPECTRUM OF THE
INNER REGION

Parameter	Best-Fit Value[a]
Power-law model:	
Photon index	2.51 (2.48–2.53)
5 mm flux[b]	3.8×10^{-12} ergs cm^{-2} s^{-1}
NEI model:	
Temperature	0.24 (0.21–0.26) keV
Abundances:[c]	
C	(<0.1)
N	(<0.03)
O	3.3 (3.0–3.5)
Ne	4.8 (4.4–5.2)
Mg	51 (42–61)
Si	131 (121–140)
S	10 (6.8–13)
Fe	37 (28–46)
$n\tau$	10.8 (9.9–11.1) $\times 10^9$ s cm^{-3}
EM[d]	2.1 (1.9–2.2) $\times 10^{55}$ cm^{-3}
Flux[b]	3.3×10^{-12} ergs cm^{-2} s^{-1}
$N_{\rm H}$	9.0 (8.5–9.4) $\times 10^{20}$ H cm^{-2}
χ_ν^2 (χ^2/dof)	447.9/215

[a] Parentheses indicate single-parameter 90% confidence regions.

[b] In the 0.3–10.0 keV band.

[c] Abundance ratio relative to the solar value (Anders & Grevesse 1989).

[d] EM $= n_e^2 V$, where n_e and V are the electron density and the volume, respectively.
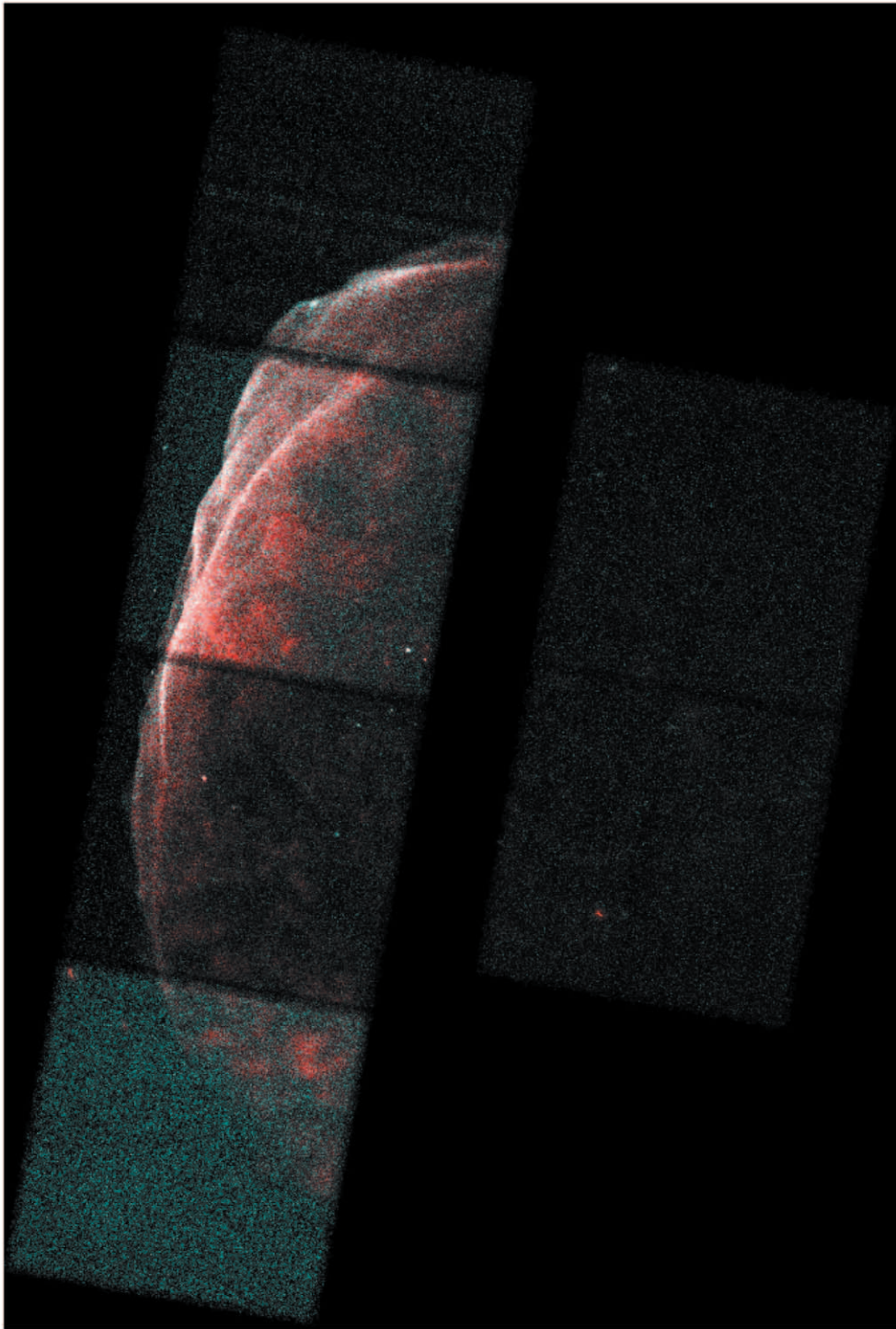
Fig. 1.—Two-color images of SN 1006 northeast shell binned with $1''$ scale. Red and blue are 0.5–2.0 keV and 2.0–10.0 keV, respectively, both in logarithmic scale.

law or *srcut* and found no essential difference from the case of an NEI model.

Although these simple models globally follow the data very well, all are rejected statistically, leaving wavy residuals near the line structure as shown in Figure 3 (*lower panel*). This may be caused by an improper response function in energy scale and/or in energy resolution. We assumed that the photons are uniformly distributed in flux and in temperature throughout the whole source region. This simple assumption may also be partly responsible for the above systematic error, because in reality the source region is apparently clumpy (see Fig. 1) and may have different temperatures, abundances, and/or ionization timescales. Since the principal aim of this paper is to examine the spatial structure and the spectra of nonthermal component, we do not examine the residuals in further detail for the thermal model. In the following analyses and discussion, we use the physical parameters cited in Table 1 as a good approximation.
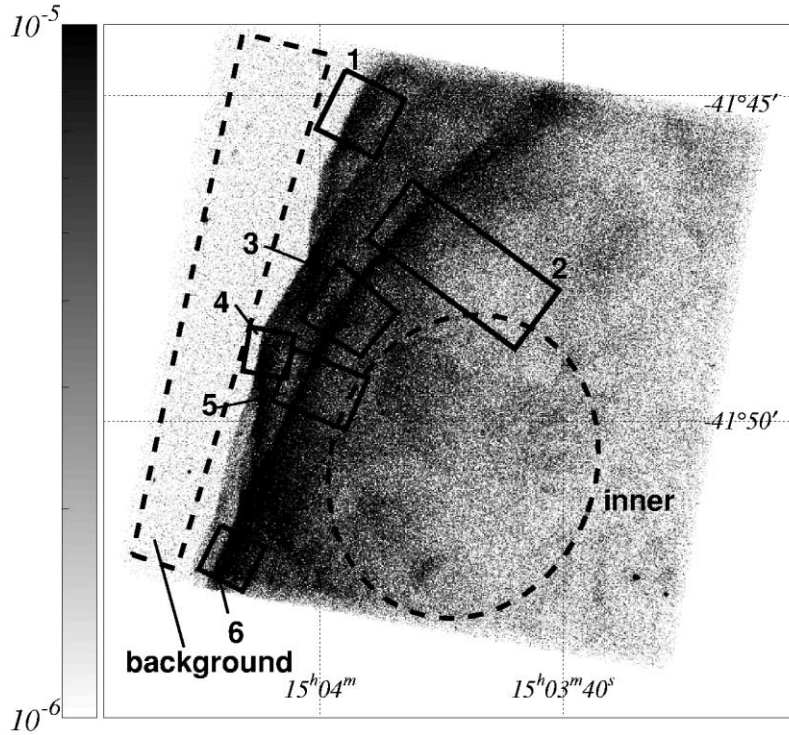
Fig. 2.—Close-up view of the 0.5–10.0 keV band image of S3 chip with J2000 coordinates, binned with $1''$ scale. The gray scale (*left bar*) is given logarithmically ranging from 1×10^{-6} to 1×10^{-5} counts s^{-1} arcsec^{-2}. The inner and background regions for the spectral analyses and the filament regions for the spatial analyses (1–6) are shown with dashed and solid lines, respectively.

The spectrum of the inner region clump is softer than that of any other region in the northeast shell, which indicates that the contribution of the thermal component is the largest. Nevertheless, the number flux of thermal photons is only 0.02% that of the nonthermal ones if we limit the energy band to 2.0–10.0 keV (the hard band); the nonthermal photons in the hard band are 8.9×10^{-2} counts s^{-1}, while thermal photons are 2.0×10^{-5} counts s^{-1}. Therefore, in the following spatial analyses, we assume that all the photons in the hard band are of nonthermal origin.

As for the spatial analysis of the thermal emission, we use the limited band of 0.4–0.8 keV (hereafter, the soft2 band)

to optimize the signal-to-noise ratio, in which K-shell lines from He-like oxygen (0.57 keV) contribute most of the X-ray emission (see Fig. 3). Even in this thermal-optimized band, however, the count rates of the thermal and nonthermal emissions are comparable: thermal photons are 8.1×10^{-1} counts s^{-1}, while those of nonthermal origin are 5.4×10^{-1} counts s^{-1}.

3.3. *The Filaments*

The outer edge of the northeast shell is outlined by several thin X-ray filaments. To study these filaments, we selected six rectangular regions in Figure 1, in which the filaments are straight and free from other structures like another filament and/or clumps. These regions are shown in Figure 2 (*solid boxes*) with the designations of 1–6 from north to south. Since the SNR shell is moving (expanding) from the right to the left, we call the right and left sides downstream and upstream, respectively, following the terminology of the shock phenomena.

Figure 4 shows the intensity profile in the hard (2.0–10.0 keV; *upper panel*) and soft2 (0.4–0.8 keV; *lower panel*) bands for each filament with the spatial resolution of $0''.5$, where the horizontal axis (x-coordinate) runs from east to west (upstream to downstream) along the line normal to the filaments. We see very fast decay on the downstream side and even faster rise on the upstream side.

To estimate the scale width, we define a simple empirical model as a function of position (x) for the profiles
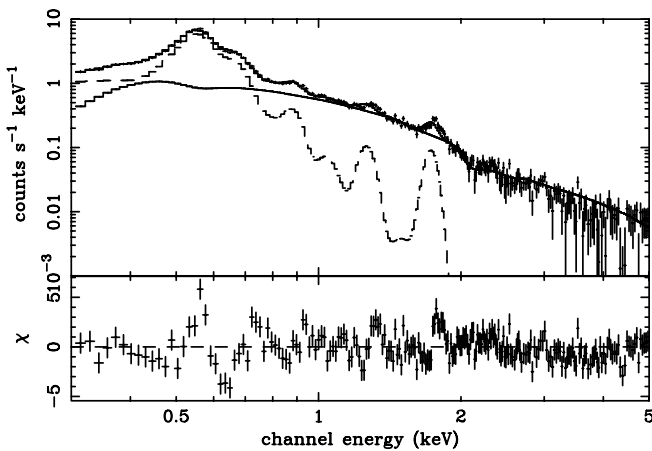

Fig. 3.—*Upper panel*: Background-subtracted spectrum of the inner region (*crosses*). Dashed line and solid lines are the best-fit thin thermal and power-law models, respectively. *Lower panel*: Data residuals from the best-fit two-component model.

$$f(x) = \begin{cases} A \exp\left|\dfrac{x_0 - x}{w_u}\right| & \text{upstream ,} \\ A \exp\left|\dfrac{x_0 - x}{w_d}\right| & \text{downstream ,} \end{cases} \quad (1)$$
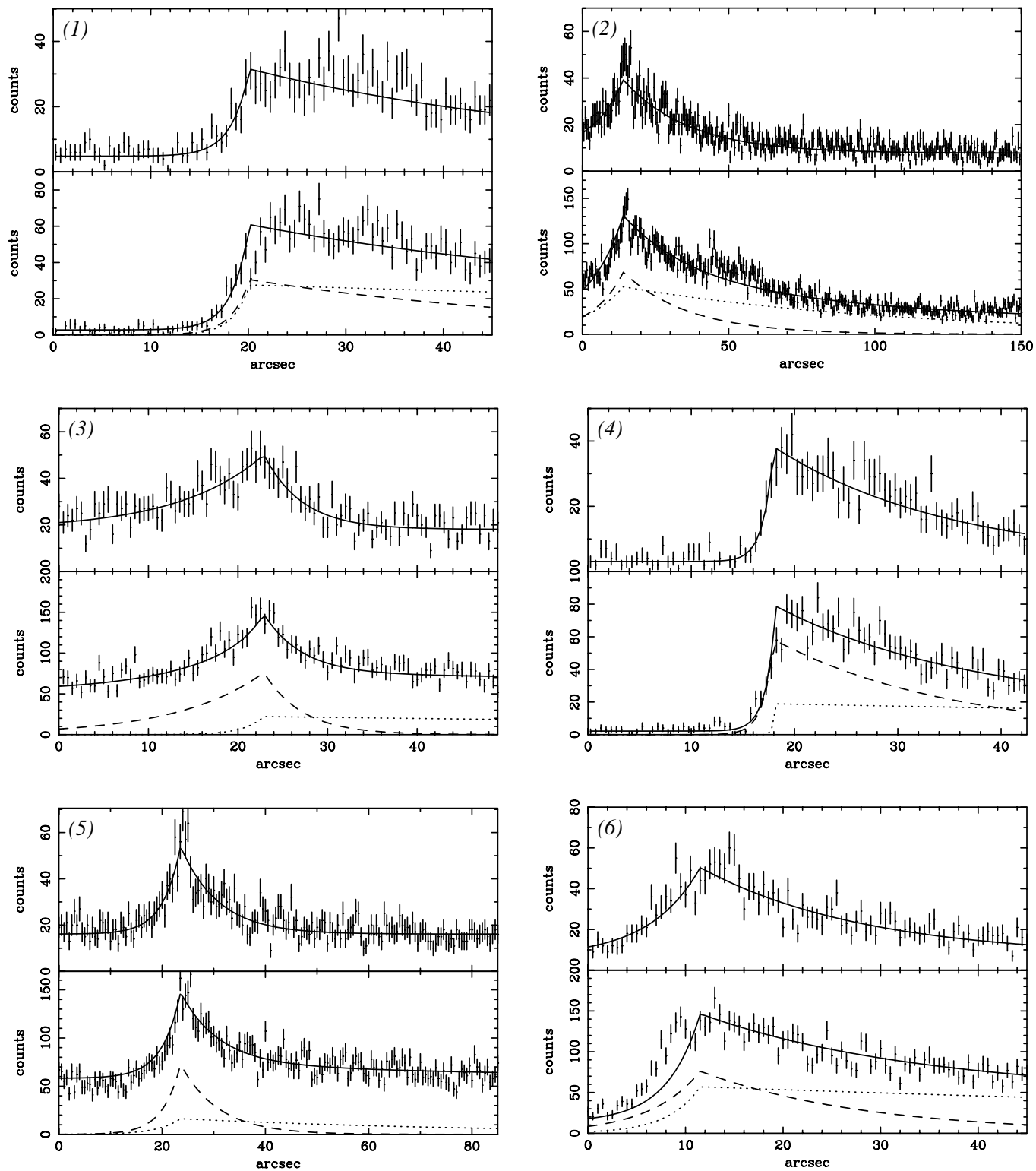
FIG. 4.—Profiles of the filaments in the SN 1006 northeast shell. Upper panels show the profiles in the hard (2.0–10.0 keV) band, whereas the lower panels in the soft2 (0.4–0.8 keV) band with the best-fit models (*solid lines*). The dashed lines in the lower panels represent nonthermal photons extrapolated from the hard band flux of the power law (*upper panels*). The dotted lines are the thermal component after subtracting the nonthermal contamination (*dashed lines*). Upstream is to the left and downstream is to the right.

TABLE 2
Best-fit Parameters of the Profiles of the Filaments

Filament No.	A^{h} [a] (counts arcsec^{-1})	w_u^h (arcsec)	w_d^h (arcsec)	χ_ν^2 (χ^2/dof)	A^{s} [b] (counts arcsec^{-1})	w_u^s (arcsec)	w_d^s (arcsec)	χ_ν^2 (χ^2/dof)
1......	53	1.9	36	119.1/105	55	1.7	1.6×10^2	104.0/94
	(49–58)	(1.3–3.0)	(30–44)	...	(49–61)	(1.3–2.2)	(>92)	...
2......	63	11	22	347.3/296	1.0×10^2	14	93	481.8/298
	(58–68)	(8.7–14)	(19–25)	...	(95–1.2×10^2)	(9.8–21)	(73–1.3×10^2)	...
3......	66	10	5.5	141.3/114	44	2.3	1.5×10^2	119.8/95
	(58–74)	(8.2–13)	(4.1–7.2)	...	(37–52)	(0.78–4.3)	(>56)	...
4......	68	0.98	18	103.2/99	38	0.12	1.5×10^2	106.1/81
	(62–74)	(0.73–1.3)	(16–21)	...	(34–42)	(Not determined)	(>78)	...
5......	75	3.8	8.0	218.3/166	33	4.5	62	236.5/167
	(66–85)	(2.8–4.9)	(6.5–9.9)	...	(24–41)	(2.2–8.7)	(43–1.0×10^2)	...
6......	87	3.5	19	99.9/86	1.1×10^2	3.4	1.3×10^2	118.4/87
	(79–96)	(2.1–5.4)	(15–26)	...	(1.0×10^2–1.3×10^2)	(2.4–5.0)	(86–2.5×10^2)	...

Note.—Parentheses indicate single-parameter 90% confidence regions.

[a] In the 2.0–10.0 keV band.

[b] In the 0.4–0.8 keV band.

where A and x_0 are the flux and position at the filament peak, respectively. The scale widths are given by w_u and w_d for upstream and downstream, respectively. Since the scale width of the filaments is larger than the spatial resolution of *Chandra* ($\sim0''\!.5$ is 1 bin in Fig. 4), we ignore the effect of the point-spread function.

3.3.1. *Nonthermal Structure*

As already noted in § 3.2, the hard band (2.0–10.0 keV) flux is of nearly pure nonthermal origin (see also the next paragraph). We therefore used the hard band profiles for the study of the nonthermal X-ray structures. The hard band profiles were fitted with a function $f^h(x) + C^h$ (superscript h designates the hard X-ray band), where C^h is the background constant, which includes the cosmic and Galactic X-ray background and non–X-ray events. The fittings were statistically accepted for all the filament profiles. The best-fit models and parameters are shown in Figure 4 (*solid lines*) and in Table 2, respectively.

We then extracted the spectra of the filaments within the scale widths ($x_0^h - w_u^h \leq x \leq x_0^h + w_d^h$) displayed in Figure 4. The background spectra were taken from the off-filament downstream regions. All the background-subtracted spectra

are featureless (no line structure) and extend to the high-energy side and were fitted with an absorbed power-law model with the best-fit parameters given in Table 3. We thus confirm that the hard X-ray profiles represent nonthermal X-rays.

To increase statistics, we summed the data of all six filaments (the combined filament). The best-fit power-law model parameters for the spectrum of the combined filament are listed in Table 3. The spectrum was also fitted with a *srcut* model (see § A1). The best-fit $\nu_{\rm rolloff}$ and the other parameters are also listed in Table 3. We note that the *srcut* model gives slightly better χ_ν^2 than does a phenomenological power-law model (see Table 3).

We further spatially divided the combined filament and analyzed each spectrum. However, we found no significant difference between the downstream and upstream regions, nor within the downstream region; the photon index was nearly constant along the x-axis in the combined filament.

3.3.2. *Thermal Structure*

To examine the structure of the thermal components, we used the soft2 band profiles (Fig. 4, *lower panels*). Contamination from the nonthermal photons would be very large

TABLE 3
Best-Fit Parameters of the Spectral Fittings for the Filaments

Parameter	Filament 1	Filament 2	Filament 3	Filament 4	Filament 5	Filament 6	Total
Power-Law Model							
Γ	2.0 (1.8–2.2)	2.4 (2.3–2.6)	2.3 (2.1–2.4)	2.3 (2.1–2.4)	2.3 (2.1–2.5)	2.3 (2.1–2.4)	2.31 (2.29–2.33)
$N_{\rm H}$ (10^{21} H cm^{-2})	1.5 (0.9–2.1)	1.8 (1.5–2.0)	1.2 (1.0–1.5)	1.6 (1.3–2.0)	1.4 (1.1–1.8)	1.4 (1.1–1.7)	1.6 (1.6–1.7)
Flux[a] (ergs cm^{-2} s^{-1})	3.7×10^{-13}	5.4×10^{-13}	3.7×10^{-13}	2.5×10^{-13}	2.3×10^{-13}	4.2×10^{-13}	1.8×10^{-12}
χ_ν^2 (χ^2/dof)	44.1/43	232.5/164	196.3/140	139.8/125	143.8/125	173.4/130	273.3/211
srcut Model							
3 mm $\nu_{\rm rolloff}$ ($\times 10^{17}$ Hz)......	13 (3.6–94)	1.7 (1.1–2.3)	2.8 (1.8–4.7)	2.9 (1.5–6.2)	2.4 (1.3–5.0)	2.8 (1.7–5.0)	2.6 (1.9–3.3)
$N_{\rm H}$ (10^{21} H cm^{-2})	1.3 (1.0–1.7)	1.4 (1.2–1.5)	1.0 (0.8–1.1)	1.3 (1.1–1.5)	1.1 (0.9–1.4)	1.1 (0.9–1.3)	1.3 (1.2–1.5)
Flux (ergs cm^{-2} s^{-1})	3.6×10^{-13}	5.3×10^{-13}	3.6×10^{-13}	2.4×10^{-13}	2.2×10^{-13}	4.1×10^{-13}	1.8×10^{-12}
χ_ν^2 (χ^2/dof)	43.7/43	225.1/164	190.9/140	139.1/125	141.1/125	170.7/130	265.2/211

Note.—Parentheses indicate single-parameter 90% confidence regions.

[a] Flux values are for the 0.3–10.0 keV band.

even in this optimized band (see § 3.2). Therefore, we calculated the flux ratio of the nonthermal photons between in the hard and soft2 bands using the spectral parameters given in Table 3. From the flux ratio and the best-fit hard band profiles, we estimated the nonthermal contaminations (Fig. 4, *dashed lines*).

After subtracting these nonthermal contaminations, we fitted the soft2 band profiles with a model of $f^s(x) + C^s$, where C^s is the background constant in the same sense as C^h. Note that although we use superscript s for the soft2 band, it actually represents thermal X-rays.

From Figure 4, we see that most of the photons at the filament peak are of nonthermal origin; hence, the statistics becomes too poor to determine the position of the thermal peak (x_0^s) independently. We thus fixed x_0^s to the best-fit peak in the hard band x_0^h. We also set the upper bound of the fitting parameter w_d^s to be 900″, the same as the radius of SN 1006 (Green 2001). The best-fit models and parameters for the thermal components $[f^s(x)]$ are shown with dotted lines in the lower panels of Figure 4 and in Table 2, respectively.

3.3.3. *Nonthermal versus Thermal*

Figure 5a shows the relation of the scale widths between the downstream and upstream sides for each filament. Although there is a large scatter, w_u is systematically smaller than w_d in both the nonthermal and thermal emissions.

Figure 5b shows the relation between w^s and w^h. We find that w_u^s is significantly larger than w_u^h, whereas w_d^s and w_u^d are comparable with each other. The mean values are $\overline{w_u^s} = 4''3 = 0.04$ pc, $\overline{w_d^s} = 1.3 \times 10^2$ arcsec $= 1.1$ pc, $w_u^h = 5''1 = 0.04$ pc, and $w_d^h = 18'' = 0.2$ pc. Note that the minimum value of w_u^h is only $0''98 = 0.01$ pc (filament 4). Perhaps their wide scatter is due to the fact that these are the projected values of the possible sheetlike structure with wavy and/or curved shapes.

4. DISCUSSION

4.1. *Thermal Plasma*

Although the best-fit NEI model in Table 1 is rejected statistically, it globally fits the thermal emission of SN 1006

as shown in Figure 3. The temperature ($kT = 0.24$ keV) is similar to the results obtained by Vink et al. (2000), Dyer et al. (2001), and Allen et al. (2001), but lower than that of Koyama et al. (1995). Since the spatial resolution of *Chandra* enables us to remove the nonthermal photons from the thermal emission more accurately than in the *ASCA* case, the present results should give a more precise description of the thermal plasma. Like the previous observations (Koyama et al. 1995; Allen et al. 2001), heavy elements, in particular iron, are overabundant, which implies that the X-ray–emitting thermal plasma is dominated by the ejecta from Type Ia SN. The fact that the thermal emission is enhanced at the inner shell region also suggests the ejecta origin.

From the emission measure (EM) and assuming a uniform density plasma of a prolate shape with the three axes of radii 140″, 120″, and 120″, we estimate the density n_e in the inner region to be 0.36 cm^{-3}. Then from the best-fit ionization parameter, τ is 2.6×10^{10} s $= 8.3 \times 10^2$ yr, roughly consistent with the age of SN 1006.

Even in the soft2 band profiles, the thermal components are not prominent (see Fig. 4), which prevents us from high-quality study of the morphology of the thermal plasma. Nevertheless, we found that the profiles of thermal filaments are largely antisymmetric. The scale width w_u^s is very sharp and comparable to w_u^h, whereas w_d^s shows a relatively large scale width. Although w_u^s couples to x_0, which is frozen to the best-fit value in the hard band (see Fig. 5b), we can say that the thermal shock has a very sharp rise in the upstream region.

The downstream scale width w_d^s is comparable to the shock width derived from the Sedov solution of about $75'' = 0.7$ pc for SN 1006 having a $15'$, or 8 pc, radius (Green 2001). Therefore, the thermal filaments may nicely trace the density profiles of the Sedov solution.

4.2. *Nonthermal Filaments*

In this section, we interpret the scale width of hard band X-rays in the upstream region, w_u^h. The hardest spectral regions, the nonthermal filaments, are the most probable site of the maximum energy acceleration. From the observation alone, we cannot judge whether the
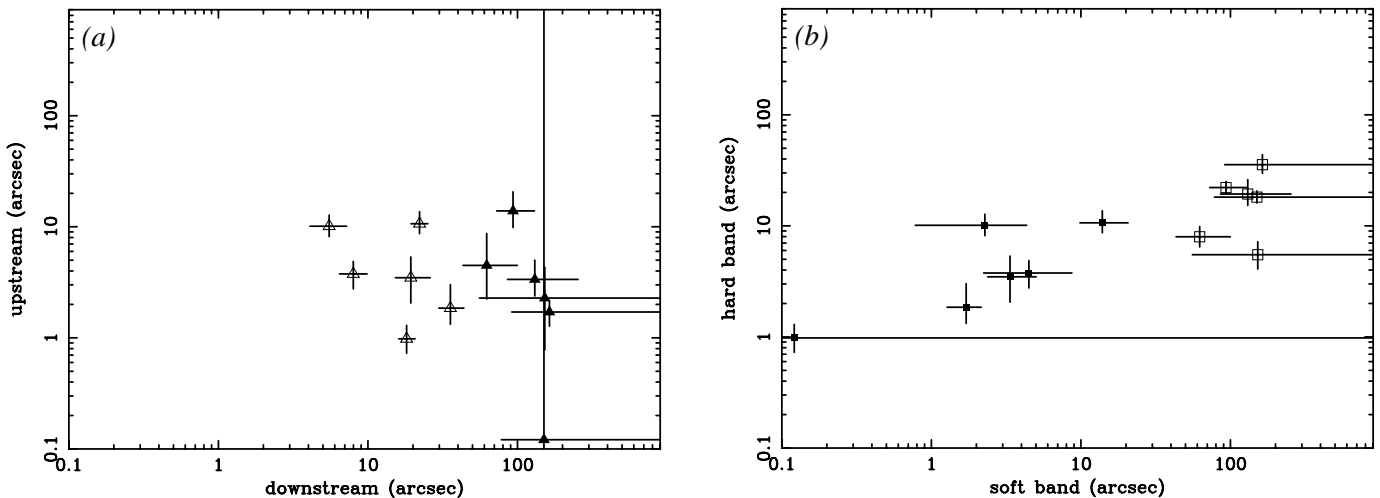

FIG. 5.—(*a*) Relation between w_u and w_d. The filled and open triangles are for the thermal and nonthermal emissions, respectively. (*b*) Relation between w^s and w^h. The filled and open boxes are in the upstream and downstream regions, respectively.

filaments are strings or sheets in edge-on configuration. Hester (1987) suggested that thin sheetlike shock fronts are seen as filaments on the edge of the SNR. The filaments seen in the figures of Hester (1987) resemble the structure in SN 1006. Furthermore, filaments should be also seen in the inner part of the shell if they are strings; however, this is not what is observed. Therefore, we assume that the filaments have sheetlike structure normal to the shock direction. The depth of the sheet is unclear but would be similar to or smaller than the length of the filament. We thus assume the depth of the sheet to be about 1 pc in the following discussion.

The most likely scenario of cosmic ray acceleration at the SNR shock is diffusive shock acceleration (DSA). The predicted results from this model, however, are highly dependent on many parameters of the magnetic field, such as the angle between the magnetic field and shock normal direction, the magnetic field strength, and its fluctuation. Here, we investigate the observed profiles based on a DSA model and estimate the physical quantities, such as diffusion coefficient, the direction of magnetic field, maximum energy of accelerated electrons, and the injection efficiency. Although a realistic condition may be more complex (as is discussed by Ellison et al. 2000 and Berezhko et al. 2002), we first apply a simple DSA model, in which the back-reaction of accelerated particles is neglected.

4.2.1. Diffusion Coefficient in the Upstream Region

The scale widths on the upstream side are largely scattered in the range of $0''.98$–$11''$ (Table 2). Since this large scatter is probably due to the projected effect of possible sheetlike structure with wavy and/or curved shape, real widths should be smaller than the observed (projected) width. To be conservative, however, we adopted the mean value of $4''.3$, or 0.04 pc at 1.8 kpc distance in the following discussion.

We use the results of srcut, the fit of the wide-band spectra from X-ray to radio band. The roll-off energy ν_{rolloff} is determined by the age of the SNR, synchrotron cooling, or diffusive escape (see § A1). The best-fit ν_{rolloff} at the filaments is $2.6^{+0.7}_{-0.7} \times 10^{17}$ Hz, which can be converted to $1.1^{+0.3}_{-0.3}$ keV. These are consistent with the ASCA results of $3.0^{+0.1}_{-0.2} \times 10^{17}$ Hz or $1.24^{+0.04}_{-0.08}$ keV by Dyer et al. (2001).

Since most of the nonthermal X-ray photons are observed in the downstream region, the synchrotron radiation is mainly due to the downstream region. Using the best-fit ν_{rolloff}, we constrain the maximum energy of electrons E_{max} and magnetic field in the downstream region B_d from equation (A6),

$$E_{\mathrm{max}} B_d^{0.5} = 0.37^{+0.04}_{-0.06} \quad \mathrm{ergs\ G^{0.5}} . \tag{2}$$

In the case of the strong shock, the magnetic field in the downstream region B_d can be related to that in the upstream region B_u as

$$B_d = \left(\cos^2 \theta_u + r^2 \sin^2 \theta_u \right)^{1/2} B_u , \tag{3}$$

where r and θ_u are the compression ratio and the magnetic field angle to the shock normal direction in the upstream region.

The diffusion coefficients in the upstream region (K_u) is estimated from equation (A9) ($u_u = u_s$) as

$$K_u \simeq w_u^h u_u = \overline{w_u^h} u_s$$
$$= 3.1 \times 10^{25} \quad \mathrm{cm^2\ s^{-1}} , \tag{4}$$

where the shock speed u_s is assumed to be 2600 km s^{-1} (Laming et al. 1996). Since the diffusion coefficient upstream is given from equation (A10), we can derive K_u for the electrons of E_{max} as

$$K_u = \frac{1}{3} \xi_u \left(\cos^2 \theta_u + \frac{\sin^2 \theta_u}{1 + \xi_u^2} \right) \frac{E_{\mathrm{max}}}{e B_u} c , \tag{5}$$

where $\xi_u (>1)$ is the fluctuation of the magnetic field.

We can derive the following expressions from equations (2), (3), (4), and (5). The maximum energy (E_{max}) and magnetic field in the upstream region (B_u) are

$$E_{\mathrm{max}} = 37 \xi_u^{-1/3} \left(\cos^2 \theta_u + \frac{\sin^2 \theta_u}{1 + \xi_u^2} \right)^{-1/3}$$
$$\times \left(\cos^2 \theta_u + r^2 \sin^2 \theta_u \right)^{-1/6} \mathrm{TeV} , \tag{6}$$

$$B_u = 4.0 \times 10^{-5} \xi_u^{2/3} \left(\cos^2 \theta_u + \frac{\sin^2 \theta_u}{1 + \xi_u^2} \right)^{2/3}$$
$$\times \left(\cos^2 \theta_u + r^2 \sin^2 \theta_u \right)^{-1/6} \mathrm{G} . \tag{7}$$

Since SN 1006 is a Type Ia SN located at a high latitude of 460 pc above the Galactic plane ($l = 14.6$ at 1.8 kpc distance), the interstellar magnetic field would be smaller than the typical value in the Galactic plane on the order of 10 μG. We therefore conservatively assume that $B_u = 10$ μG, which is slightly larger than the combined results of the X-ray and TeV gamma rays (Tanimori et al. 2003). Then equation (7) becomes

$$\xi_u^{2/3} \left(\cos^2 \theta_u + \frac{\sin^2 \theta_u}{1 + \xi_u^2} \right)^{2/3} \left(\cos^2 \theta_u + r^2 \sin^2 \theta_u \right)^{-1/6} = 0.25 . \tag{8}$$

For the parallel magnetic field ($\theta_u = 0°$), ξ_u becomes smaller than 1. This unrealistically small value of ξ_u conflicts with a usual DSA, in which a parallel magnetic field configuration is assumed.

An alternative scenario is a magnetic field oblique to the shock normal in this region ($\theta_u > 0°$). For simplicity, we neglect the back-reaction of accelerated particle, and the compression ratio becomes 4 in the strong shock limit. The allowed region of θ_u is given from equation (8) as

$$\theta_u \geq 82° . \tag{9}$$

Thus, the magnetic field in the upstream region near the filaments is almost perpendicular.

Assuming $\theta_u = 90°$, $r = 4$, and $B_u = 10$ μG, E_{max} is given from equation (6):

$$E_{\mathrm{max}} = r^{-1/2} B_u^{-1/2} 0.23^{+0.03}_{-0.04} \mathrm{TeV}$$
$$= 37^{+4}_{-7} \mathrm{TeV} . \tag{10}$$

When particles are accelerated very efficiently, their back-reactions to the shock cannot be ignored; hence, r becomes

larger than 4. Even if the compression ratio is $r = 7$, which is the typical value for a shock strongly modified by accelerated particles (Ellison et al. 2000; Berezhko et al. 2002), the allowed range is $\theta_u > 80°$. Therefore, we can safely predict that the magnetic field in the northeast shell of SN 1006 is nearly perpendicular to the shock normal.

As for the downstream region, the observed spatial profile seems to be incompatible with the solution derived by Blandford & Ostriker (1978). The maximum electron energy E_{max} would be determined by the balance of the timescales between the accelerating and the synchrotron cooling. These timescales may depend on the structure and the fluctuation of the magnetic field along the shock normal; both timescales become smaller with larger magnetic field, while the former might become even smaller with larger fluctuation of the magnetic field.

The shock flow compresses and partly stretches the magnetic field in the radial direction, which may produce a highly disordered magnetic field with a small fraction of the radial component, as discussed by Reynolds & Gilmore (1993), who analyzed the radio polarization data and reported that only 15%–20% of the magnetic field energy in SN 1006 northeast shell is in radial polarization, and most of the magnetic field is disordered on a scale smaller than 0.2 pc.

To determine the magnetic field in the downstream region, we need more information on such complicated effects as the history of the shock propagation and the nonlinear effects, and to make many other assumptions, which are beyond this paper and which we leave to a future study.

4.2.2. Injection Efficiency

We define the injection efficiency $\eta \equiv n_e^{NT}/n_e^T$, where n_e^{NT} and n_e^T are the number densities of nonthermal and thermal electrons in the filaments. The depth of the filament (sheetlike) is assumed to be 1 pc (see § 4.2.1), with uniform electron density.

The nonthermal electron flux (energy) is estimated using the method given in the Appendix (§ A1), where the nonthermal X-ray flux and spectra of each filament are taken from Tables 2 and 3. We adopt the minimum energy of nonthermal electrons (injection energy) E_{min} to be 0.24 keV (the

temperature of the thermal plasma; see Table 1). The magnetic field and the maximum energy are unknown parameters; however, we can suggest that the magnetic field in the downstream region is significantly larger than that in the upstream region. In this section, we adopt the magnetic field B to be perpendicular to the shock normal, $B_d = 4B_u = 40$ μG (chosen as a typical value) and the maximum energy E_{max} to be 37 TeV from the discussion in § 4.2.1. The derived number density (n_e^{NT}), the total number (N_e^{NT}), and the total energy (E_e^{NT}) of nonthermal electrons in each filament are summarized in Table 4.

For the estimation of the thermal electron flux (energy), we adopted the projected profile of the thermal X-rays (the soft2 band) given in Table 2 and the spectral parameters of thermal plasma given in Table 3. The resultant number density (n_e^T), total number (N_e^T), and total energy (E_e^T) of thermal electrons in each filament are given in Table 4. The injection efficiency η ($\equiv n_e^{NT}/n_e^T$) is then obtained as is shown in Table 4. All the values η are nearly identical in each filament of $\sim 1 \times 10^{-3}$ but are about 2 times larger than the value 5×10^{-4} derived from the ASCA data by Allen et al. (2001), although they also assumed $B_d = 40$ μG. For comparison, we estimate η with a larger magnetic field of $B_d = 40$ μG, and find a larger η than did Allen et al. (2001). They estimated the number density of nonthermal electrons from larger regions than the filaments because ASCA could not resolve the filaments. On the other hand, we found that the nonthermal electrons are confined in the thin filaments, which are the sites of ongoing acceleration of the nonthermal electrons. We thus regard that the present Chandra result suggests that the injection occurs more locally and more efficiently, and as a result, it must be a more realistic estimation of η than that by Allen et al. (2001).

The energy densities of the magnetic field, the thermal plasma, and the nonthermal electrons in the filaments are 6.4×10^{-11}, 2.6×10^{-10}, and 6.9×10^{-11} ergs cm^{-3}, respectively. Thus, at the shocked region, the magnetic field and nonthermal electrons are in energy equipartition and are slightly smaller than the thermal energy (about 30%).

As suggested by Ellison et al. (2000), the nonthermal protons should carry larger energy than electrons, and hence particle energy becomes larger than that of magnetic and possibly that of thermal. We therefore must consider

TABLE 4

NUMBER DENSITIES AND ENERGIES OF THERMAL AND NONTHERMAL ELECTRONS

Parameter	Filament 1	Filament 2	Filament 3	Filament 4	Filament 5	Filament 6	Total
Thermal Electrons							
EM (cm^{-3})	7.0×10^{53}	1.0×10^{54}	1.3×10^{53}	2.5×10^{53}	1.3×10^{53}	8.4×10^{53}	3.1×10^{54}
Density[a] (n_e^T) (cm^{-3})..........	0.43	0.51	0.26	0.41	0.30	0.60	0.45
Total number (N_e^T)............	1.6×10^{54}	2.1×10^{54}	5.0×10^{53}	6.1×10^{53}	4.3×10^{53}	1.4×10^{54}	6.8×10^{54}
Energy (E_e^T)[b] (ergs)............	9.2×10^{44}	1.2×10^{45}	2.8×10^{44}	3.5×10^{44}	2.4×10^{44}	7.9×10^{44}	3.9×10^{45}
Nonthermal electrons[c]							
Density (n_e^{NT})[a] (cm^{-3})........	4.7×10^{-4}	5.5×10^{-4}	7.9×10^{-4}	7.1×10^{-4}	6.5×10^{-4}	7.6×10^{-4}	6.2×10^{-4}
Total number (N_e^{NT})..........	1.8×10^{51}	2.2×10^{51}	1.5×10^{51}	1.1×10^{51}	9.4×10^{50}	1.8×10^{51}	9.3×10^{51}
Energy (E_e^{NT}) (ergs)...........	2.0×10^{44}	2.4×10^{44}	1.7×10^{44}	1.2×10^{44}	1.1×10^{44}	2.0×10^{44}	1.0×10^{45}
Injection efficiency (η[d])	1.1×10^{-3}	1.1×10^{-3}	3.0×10^{-3}	1.7×10^{-3}	2.2×10^{-3}	1.3×10^{-3}	1.4×10^{-3}

[a] We assumed that the depth of the emitting volume is 1 pc and that the filling factor is 1.
[b] $E_e^T = \frac{3}{2} n_e V^{NT} kT$.
[c] Integration from $E_{min} = 0.24$ keV to $E_{max} = 37$ TeV (see text).
[d] $\eta \equiv n_e^{NT}/n_e^T$ (see text).

nonlinear effects suggested by Ellison et al. (2000) and by Berezhko et al. (2002); however, a more quantitative scenario including the nonlinear effects must be a future work.

5. SUMMARY

1. X-ray emissions from the northeast shell of SN 1006 are found to be composites of filaments, clumps, and more extended diffuse emissions. We resolved the thermal and nonthermal X-rays using the different spectral shape and morphology.

2. The spectrum of the thermal component has temperature $kT = 0.24$ keV and a relatively small ionization timescale $n_e\tau = 1.1 \times 10^{10}$ s cm^{-3}. The chemical compositions are overabundant, especially in iron, which suggests that the X-ray–emitting plasma originates from ejecta and the progenitor is Type Ia.

3. The nonthermal components can be described by a power-law function with photon index 2.1–2.3 in the narrow filaments and 2.5 at the inner region of the shell.

4. The structure of the filaments shows different characteristics in thermal and nonthermal X-rays. The thermal plasma has a scale width of 1 pc in the downstream region, similar to the shock width derived from Sedov equations. The nonthermal filaments show extremely small scale width of $w_u^h \sim 0.04$ pc and $w_d^h \sim 0.2$ pc upstream and downstream, respectively.

5. In a diffusive shock acceleration model, the observed thin filaments require a magnetic field nearly perpendicular to the shock normal, with the angle larger than ~80° (the magnetic field in the upstream region is assumed to be 10 μG). . The maximum energy of the electrons is 30–40 TeV.

6. The injection efficiency is estimated to be $\eta = 1 \times 10^{-3}$, suggesting that thermal particles are injected locally and very effectively. Then the energy density of nonthermal electrons becomes comparable to that of the magnetic field and about 30% of the thermal energy density. Thus, nonlinear effects of the shock structure and acceleration mechanism must be considered.

APPENDIX

In this appendix, we briefly introduce the relevant software tools and equations, which are used for the discussions in the text.

A1. ELECTRON SPECTRA AND *srcut* MODEL

The spectrum of nonthermal electrons accelerated by the diffusive shock is (Bell 1978)

$$\frac{dn_e^{\mathrm{NT}}}{dE^{\mathrm{NT}}} = \kappa(E^{\mathrm{NT}} + m_e c^2)[(E^{\mathrm{NT}})^2 + 2m_e c^2 E^{\mathrm{NT}}]^{-(p+1)/2} \exp\left(\frac{-E^{\mathrm{NT}}}{E_{\max}}\right), \tag{A1}$$

where n_e^{NT} and E^{NT} are the number density and the energy of nonthermal electrons, respectively.

The synchrotron radiation power per unit frequency from a single electron of energy E in a magnetic field B is

$$P(\nu, \alpha) = \frac{\sqrt{3}e^3 B \sin\alpha}{m_e c^2} F\left(\frac{\nu}{\nu_c}\right), \tag{A2}$$

where α and $F(x)$ are the pitch angle and the function given by Rybicki & Lightman (1979). The peak frequency ν_c is

$$\nu_c = \frac{3cE^2 eB \sin\alpha}{4\pi(m_e c^2)^3}. \tag{A3}$$

Convolving equation (A1) with equation (A2), we obtain the spectrum of synchrotron radiation in the pitch angle α as

$$f(\nu, \alpha) = \int_{E_{\min}}^{\infty} dE^{\mathrm{NT}} \frac{dn_e^{\mathrm{NT}}}{dE_e^{\mathrm{NT}}} P(\nu, \alpha). \tag{A4}$$

Averaged over the pitch angle, we finally obtain the synchrotron radiation energy per unit volume, frequency, and time,

$$f(\nu) = \frac{1}{2} \int_0^{\pi} d\alpha \sin\alpha f(\nu, \alpha). \tag{A5}$$

The observed spectrum is fitted with this model spectrum using the *Chandra* software *srcut* with three free parameters (Reynolds 1998; Reynolds & Keohane 1999). The normalization constant and spectral index are determined so as to reproduce the flux and slope in the radio band. These parameters are converted to κ and p in equation (A1). The other fitting parameter ν_{rolloff} is a function of $E_{\max}$ in equation (A1) and magnetic field (B) (Reynolds & Keohane 1999)

$$\nu_{\mathrm{rolloff}} = 0.5 \times 10^{16} \left(\frac{B}{10 \ \mu\mathrm{G}}\right)\left(\frac{E_{\max}}{10 \ \mathrm{TeV}}\right)^2 \ \mathrm{Hz}. \tag{A6}$$

This equation gives constraint on the maximum electron energy $E_{\max}$ and the magnetic field B.

Since available radio data of SN 1006 have spatial resolution far larger than the scale of the X-ray filaments, we have no accurate radio flux nor index from the position of the X-ray filaments. We therefore fixed the radio index to the poor-resolution radio result of $p = 2.14$ by Allen et al. (2001), and the radio flux is treated as a free parameter for the present *srcut* fitting. Allowing the radio index to vary from $p = 2.0$ to 2.2, we see no significant difference in the best-fit parameters within the statistical errors.

A2. DIFFUSION VERSUS ADVECTION

The spatial structure of the relativistic electrons produced by the diffusive shock acceleration across the shock is determined by the competing processes of diffusion and advection. The advection timescale ($\tau_{\rm ad}$) is given by

$$\tau_{\rm ad} = \frac{w}{u} \ , \tag{A7}$$

where w is the scale width of the spatial distribution of the relativistic electrons and u is the flow speed.

The diffusion timescale ($\tau_{\rm dif}$) is given from the random-walk theory as

$$\tau_{\rm dif} = \frac{w^2}{K} \ , \tag{A8}$$

where K is the diffusion coefficient.

In order for the high-energy electrons to be accelerated at the shock front, electrons in the upstream region should be diffused back to the shock front against the advection in the downstream side with fluid speed u_d. Therefore, $\tau_{\rm ad}$ should be nearly equal to $\tau_{\rm dif}$; hence $w_u/u_u \simeq w_u^2/K_u$. We thus obtain

$$w_u \simeq \frac{K_u}{u_u} \ . \tag{A9}$$

For more exact formalisms, see, e.g., Bell (1978), Blandford & Ostriker (1978), and Drury (1983).

Let the mean free path parallel to the magnetic field be a constant factor ξ times the gyroradius r_g. Then, the effective diffusion coefficient along the shock normal is given as (Jokipii 1987; Skilling 1975)

$$K = \frac{1}{3} \xi r_g c \left(\cos^2 \theta_u + \frac{\sin^2 \theta_u}{1 + \xi^2} \right) \ , \tag{A10}$$

$$r_g = \frac{E_e}{eB} \ , \tag{A11}$$

where e, E_e, B, and θ_u are the electric charge, the energy of relativistic electrons, the magnetic field, and the angle between the magnetic field upstream and the shock normal, respectively.

REFERENCES

Aharonian, F. A., & Atoyan, A. M. 1999, A&A, 351, 330
Allen, G. E., Petre, R., & Gotthelf, E. V. 2001, ApJ, 558, 739
Anders, E., & Grevesse, N. 1989, Geochim. Cosmochim. Acta, 53, 197
Bamba, A., Tomida, H., & Koyama, K. 2000, PASJ, 52, 1157
Bell, A. R. 1978, MNRAS, 182, 443
Berezhko, E. G., Ksenofontov, L. T., & Völk, H. J. 2002, A&A, 395, 943
Blandford, R. D., & Eichler, D. 1987, Phys. Rep., 154, 1
Blandford, R. D., & Ostriker, J. P. 1978, ApJ, 221, L29
Borkowski, K. J., Lyerly, W. J., & Reynolds, S. P. 2001a, ApJ, 548, 820
Borkowski, K. J., Rho, J., Reynolds, S. P., & Dyer, K. K. 2001b, ApJ, 550, 334
Drury, L. O'C. 1983, Rep. Prog. Phys., 46, 973
Dyer, K. K., Reynolds, S. P., Borkowski, K. J., Allen, G. E., & Petre, R. 2001, ApJ, 551, 439
Ellison, D. C., Berezhko, E. G., & Baring, M. G. 2000, ApJ, 540, 292
Enomoto, R., et al. 2002, Nature, 416, 823
Garmire, G., Feigelson, E. D., Broos, P., Hillenbrand, L. A., Pravdo, S. H., Townsley, L., & Tsuboi, Y. 2000, AJ, 120, 1426
Green, D. A. 2001, A Catalogue of Galactic Supernova Remnants (2001 December Version), (Cambridge: Mullard Radio Astron: Obs)
Hess, V. F. 1912, Phys. Z., 13, 1084
Hester, J. J. 1987, ApJ, 314, 187
Jokipii, J. R. 1987, ApJ, 313, 842
Jones, F. C., & Ellison, D. C. 1991, Space Sci. Rev., 58, 259
Koyama, K., Kinugasa, K., Matsuzaki, K., Nishiuchi, M., Sugizaki, M., Torii, K., Yamauchi, S., & Aschenbach, B. 1997, PASJ, 49, L7

Koyama, K., Petre, R., Gotthelf, E. V., Hwang, U., Matsura, M., Ozaki, M., & Holt, S. S. 1995, Nature, 378, 255
Laming, J. M., Raymond, J. C., McLaughlin, B. M., & Blair, W. P. 1996, ApJ, 472, 267
Malkov, M., & Drury, L. O'C. 2001, Rep. Prog. Phys., 64, 429
Morrison, R., & McCammon, D. 1983, ApJ, 270, 119
Muraishi, H., et al. 2000, A&A, 354, L57
Reynolds, S. P. 1998, ApJ, 493, 375
Reynolds, S. P., & Gilmore, D. M. 1993, AJ, 106, 272
Reynolds, S. P., & Keohane, J. W. 1999, ApJ, 525, 368
Rybicki, G. B., & Lightman, A. P. 1979, Radiative Processes in Astrophysics (New York: Wiley Interscience)
Skilling, J. 1975, MNRAS, 172, 557
Slane, P., Gaensler, B. M., Dame, T. M., Hughes, J. P., Plucinsky, P. P., & Green, A. 1999, ApJ, 525, 357
Slane, P., Hughes, J. P., Edgar, R. J., Plucinsky, P. P., Miyata, E., Tsunemi, H., & Aschenbach, B. 2001, ApJ, 548, 814
Tanimori, T., et al. 1998, ApJ, 497, L25
———. 2003, in Proc. 27th Int. Cosmic Ray Conf. (Hamburg), 2465
Vink, J., Kaastra, J. S., Bleeker, J. A. M., & Preite-Martinez, A. 2000, A&A, 354, 931
Weisskopf, M. C., O'Dell, S. L., & van Speybroeck, L. P. 1996, Proc. SPIE, 2805, 2
Winkler, P. F., & Long, K. S. 1997, ApJ, 491, 829